Applied Catalysis A, General 593 (2020) 117441

Contents lists available at ScienceDirect

Applied Catalysis A, General

journal homepage: www.elsevier.com/locate/apcata

Cobalt nanocrystals on carbon nanotubes in the Fischer-Tropsch synthesis: Impact of support oxidation

T.W. van Deelen[a], H. Yoshida[a,b], R. Oord[a], J. Zečević[a], B.M. Weckhuysen[a], K.P. de Jong[a,*]

[a] Inorganic Chemistry and Catalysis, Debye Institute for Nanomaterials Science, Utrecht University, Universiteitsweg 99, 3584 CG, Utrecht, the Netherlands
[b] The Institute of Scientific and Industrial Research, Osaka University, 8-1 Mihogaoka, Ibaraki, Osaka, 567-0047, Japan

ARTICLE INFO

Keywords:
Carbon nanotubes
Functionalization
Cobalt
Nanocrystals
Fischer-Tropsch synthesis

ABSTRACT

The effect of oxidation of a carbon nanotube (CNT) support on the structure and catalytic performance in the Fischer-Tropsch (FT) synthesis of pre-synthesized cobalt nanocrystals (NC) has been investigated. 6 nm CoO-NC were prepared using colloidal techniques and impregnated on pristine and surface-oxidized CNT. The CoO-NC on pristine CNT were reduced completely to Co, while ~50 % CoO reduction was observed on oxidized CNT (oxCNT), indicating a stronger Co-support interaction on oxCNT. In FT, the turnover frequency (TOF) after 100 h was exceptionally high on pristine CNT ($150{\cdot}10^{-3}$ s^{-1}) against $63{\cdot}10^{-3}$ s^{-1} on oxCNT. In the initial stage of FT, the TOF was 35 % lower on oxCNT than on pristine CNT, which matched with 32 % lower crystallinity of cobalt determined using in situ XRD. Furthermore, deactivation was observed mainly on oxCNT. These results demonstrate the large impact of the support on the structure and performance of nanocrystal-based catalysts.

1. Introduction

Current energy scenarios call for more sustainable and versatile supply of transportation fuels [1] and, at the same time, the demand for liquid fuels is expected to grow in the coming years [2]. To solve this conundrum, so-called XTL technology (X-to-liquids, with X being biomass, municipal waste, natural gas or coal) in particular when combined with carbon capture and storage can be instrumental as a versatile and efficient method of producing liquid fuels. At the heart of this technology is the Fischer-Tropsch (FT) synthesis, i.e. the catalytic conversion of synthesis gas (an H_2/CO mixture) to hydrocarbons that serve as synthetic fuels [3]. Currently, FT produces more than half a million barrels of synthetic fuel per day [4] (against roughly 100 million barrels per day produced from crude oil [5]) and most modern FT plants apply cobalt-based catalysts, especially for gas-to-liquids (GTL) [4]. In these catalysts, the cobalt, being relatively expensive, is typically used as efficiently as possible by nanosizing the cobalt particles to optimize their surface-to-volume ratio [6]. Such nanosized cobalt nanoparticles are dispersed on a support to prevent cobalt aggregation and to provide mechanical stability to the overall catalyst [7]. The most frequently applied supports for cobalt-based FT catalysts are oxidic compounds, such as Al_2O_3, SiO_2 or TiO_2, which usually interact with cobalt and influence the FT performance [8]. Carbon supports, on the other hand, present an interesting alternative, especially for fundamental studies, given their chemical inertness (limited or no cobalt-support compound formation).

Various types of carbon have been applied as supports [9], including activated carbon, ordered mesoporous carbon [10], and carbon nanofibers [11,12] and carbon nanotubes [13]. Among these, carbon nanotubes (CNT) have an open, macro- and mesoporous structure combined with a high specific surface area [14]. Moreover, the surface of pristine CNT contains a low amount of functional groups, rendering these hydrophobic [15]. To increase hydrophilicity, oxygen-containing functional groups can be introduced by oxidation of pristine CNT, for example using nitric and/or sulfuric acid [15,16]. Functional groups can also act as anchoring sites for metal nanoparticles and hence, metals supported on oxidized CNT (oxCNT) typically display increased resistance towards sintering under reaction conditions [17].

Several groups reported higher activity for Co/oxCNT compared to Co/CNT, while C_{5+}-selectivity decreased with CNT oxidation [18–20]. Interestingly, Eschemann et al. [13] showed that CNT functionalization has a major effect on the FT performance of Co/CNT catalysts, with significantly lower activity and C_{5+}-selectivity for oxCNT. The different catalytic performance was tentatively ascribed to an increase in hcp Co on pristine CNT compared to oxCNT, as observed by in situ XRD during reduction, because often hcp Co is more active in FT than fcc Co [21–25]. However, the exact nature of the differences between Co supported on CNT and oxCNT was not established.

* Corresponding author.
E-mail address: k.p.dejong@uu.nl (K.P. de Jong).

https://doi.org/10.1016/j.apcata.2020.117441
Received 11 November 2019; Received in revised form 25 January 2020; Accepted 27 January 2020
Available online 30 January 2020

More insight into the metal-support interaction after support functionalization and its effect in FT could potentially be obtained by using better defined catalysts in combination with advanced characterization techniques. Colloidal techniques offer the possibility to synthesize metal nanocrystals (NC) separately with high precision in e.g. NC size, shape or crystal structure [26]. In the case of Co-NC, low-temperature oxidation to CoO facilitates their subsequent uniform attachment and ligand removal during reduction [27]. Because NC synthesis is decoupled from attachment to the support, the starting cobalt particles should be very similar, meaning that differences in FT must be caused by altered metal-support interactions related to functionalization of the CNT.

In this work, we have investigated the effect of CNT surface oxidation on the structure and catalytic performance of CNT-supported cobalt nanocrystals in the Fischer-Tropsch synthesis. Catalyst were prepared via colloidal synthesis of 6 nm CoO-NC and subsequent attachment to CNT and oxCNT. CNT oxidation resulted in decreased reducibility and sintering propensity of the cobalt (oxide) phase during reduction. In FT, Co-NC on pristine CNT were highly active, while the activity on oxCNT was approximately a factor two lower. Using in situ XRD, the crystalline metallic Co content on oxCNT was found to be 32 % lower than on pristine CNT, making it the most probable cause for the observed 35 % lower initial TOF on oxCNT. Catalyst deactivation during FT occurred mainly on oxCNT, while particle growth, NC restructuring, or oxidation were excluded as deactivation mechanisms, leaving enhanced carbon deposition as one of the few likely options.

2. Experimental methods

2.1. CNT oxidation

Oxidized CNT (oxCNT) were obtained by heating 4 g CNT (Baytubes c150 HP, purity > 99 %, remaining metals encapsulated) in 150 mL concentrated HNO_3 at 80 °C for 90 min. Afterwards, the oxCNT was washed on a vacuum filtration setup with 2.5 L deionized H_2O until the pH of the filtrate reached 5. The washed oxCNT was dried at 120 °C in static air overnight.

2.2. Synthesis of cobalt nanocrystals

The colloidal synthesis of cobalt nanocrystals (Co-NC) was based on a previously reported method [28], which was selected because the use of phosphorus-containing ligands was avoided. The synthesis was performed under N_2 atmosphere on a Schlenk line. Typically, 65 mg of oleic acid (Sigma-Aldrich, 90 %, technical grade) was transferred to a 100 mL 3-necked flask equipped with a cooler and two septa and evacuated at 100 °C for 30 min. After flushing several times with N_2, 7.5 mL of 1,2-dichlorobenzene (Sigma-Aldrich, 99 %, anhydrous) was transferred under N_2 to the flask and the mixture was heated to 174 °C under 750 rpm magnetic stirring. Meanwhile, 270 mg dicobalt octacarbonyl (Acros Organics, 95 %, stabilized) was dissolved in 1.5 mL 1,2-dichlorobenze inside a glovebox. When the solution in the flask reached 174 °C, the cobalt precursor was rapidly injected into the flask. The solution was left to react for 20 min and quenched afterwards using a water bath. The Co-NC suspension was exposed to air for one hour at room temperature under 650 rpm magnetic stirring to convert Co-NC to CoO-NC. Subsequently, the colloidal CoO dispersion was transferred to glass centrifuge tubes, filled up to 20 mL with 2-propanol (Sigma-Aldrich, > 99 %, LC–MS Chromasolv) and centrifuged at 2200 G for 20 min. The supernatant was decanted and the precipitated CoO-NC were re-dispersed in n-hexane (Acros Organics, 99+ %) using sonication. This washing cycle with 2-propanol was repeated 3 times more and finally the NC were re-dispersed in 2 mL toluene (Acros Organics, 99+ %, extra pure) and stored in a glass vial.

2.3. Attachment of cobalt oxide nanocrystals on CNT and oxCNT

The supports were sieved to a grain size of 75 − 150 μm prior to being used. Attachment of 10 wt% of CoO-NC on CNT and oxCNT was performed by pore-filling impregnation with the colloidal dispersion. For this, the (ox)CNT were dried at 80 °C under vacuum for 1 h. After cooling to room temperature, 2.5 mL·$g_{support}^{-1}$ of colloidal dispersion in toluene, equivalent to the pore volume of (ox)CNT, was injected to the support under magnetic stirring. The toluene evaporated upon contact with the vacuum, immediately emptying the syringe. After mixing, the sample was dried at 60 °C for 1 h in static air, 120 °C for 3 h in static air and 80 °C for 3 h under vacuum.

2.4. Characterization

CNT and oxCNT were titrated using a Radiometer Analytical TitraLab TIM880 automatic titration setup. Between 25 − 30 mg of sample was suspended in 30 mL 0.1 M KCl by sonication, flushed for 10 min with N_2 to remove CO_2 and subsequently titrated with 0.01 M NaOH in 0.1 M KCl under N_2 atmosphere. The data was analyzed as described by Eschemann et al. [13], i.e. a second-degree equation ($y = ax^2 + bx + c$) was fitted to the first derivative of the pH curve and the inflection point was calculated using $x_{inflection} = -b/2a$.

N_2-physisorption was measured on a Micromeritics Tristar 3000. The samples were pre-dried under N_2 flow at 120 °C for 80 h for CNT and 150 °C for 20 h for oxCNT. Both samples were analyzed over P/P_0 = 0-0.995 at −196 °C. The surface area was determined using the BET method and the mesopore volume by single point analysis of the desorption isotherm at $P/P_0 = 0.995$.

Transmission electron microscopy (TEM) was performed on an FEI Tecnai 12 operating at 120 kV. Scanning transmission electron microscopy with energy-dispersive X-ray spectroscopy (STEM-EDX) was performed in high-angle annular dark-field (HAADF) mode on a Talos F200X (Thermo Fisher Scientific). The microscope was equipped with a high-brightness field emission gun (X-FEG) and a Super-X G2 EDX detector and was operated at 200 kV. Samples of colloidal dispersions in hexane were prepared by drop casting on a carbon coated Cu grid. In the case of supported catalysts, the powder was first suspended in 2-propanol by sonication and subsequently drop casted on a holey carbon coated Cu grid. The particle sizes were manually determined using iTEM software and at least 200 particles were analyzed to allow a statistical analysis. All reported particle sizes were recalculated to equivalent metallic Co size by correcting for the lattice expansion of a 3 nm CoO passivation layer (Co-NC and reduced/spent catalysts). All particle sizes are reported as volume/surface mean diameter (D[3,2]).

Inductively coupled plasma-optical emission spectroscopy (ICP-OES) was measured on a SPECTRO ARCOS and samples were prepared by cobalt extraction in aqua regia.

Temperature programmed reduction (TPR) was measured using a Micromeritics AutoChem 2920. 25 mg of sample was reduced by heating to 800 °C with 5 °C min^{-1} in a flow of 5 vol% H_2 in Ar.

X-ray diffraction (XRD) was performed on a Bruker D2 Phaser using Co radiation (Kα1 1.789 Å). The diffractograms were analyzed and fitted using Bruker's Eva and Topas software. After fitting the full scan from 20 to 100 ° 2θ, the crystallite size was calculated using the Scherrer equation to analyze the CoO [111] peak.

In situ XRD patterns were measured on a Bruker D8 Discover with a Mo (Kα1 0.709 Å) source in Debye-Scherrer transmission (capillary) geometry. The X-ray beam was focused on a quartz capillary with 1000 μm OD and a wall thickness of 10 μm using a Göbel-mirror. The setup was equipped with an energy dispersive LynxEye XE Position Sensitive Detector (PSD). Details on the complete setup can be found in recent publications [29,30]. The patterns were measured between 9 and 39° 2θ with an increment of 0.07° and time per step of 15.3 s. Multiple scans were accumulated to improve the signal-to-noise ratio only if the patterns were identical. Rietveld Quantitative Phase Analysis

(Rietveld QPA) was performed on the measured diffractograms using Bruker TOPAS (v5) software. Details of the Rietveld refinement procedure are given in Supplementary Methods. Typically, 3.5 mg sample in the sieve fraction 75 − 150 μm was loaded in the capillary and fixed with quartz wool at either end, resulting in a catalyst bed length of ~20 mm. The capillary was placed in the setup and the catalysts were reduced in situ at 350 °C for 8 h (1 °C min^{-1}) in a 1.2 mL·min^{-1} flow of 25 vol% H_2 in He at 1 bar. After reduction, the temperature was lowered to 180 °C with 3 °C min^{-1} and at this temperature, a 3.0 mL min^{-1} flow of synthesis gas H_2/CO = 2 (v/v) was introduced. After 10 min stabilization, the back-pressure regulator was set to 10.6 bar. Only after the pressure was reached and stable, the temperature was increased to 220 °C with 1 °C min^{-1}, which was defined as TOS = 0 h. In situ XRD patterns were recorded both during reduction and FT.

2.5. Fischer-Tropsch synthesis

The performance of the catalysts was evaluated using an Avantium Flowrence 16 parallel reactor setup. Stainless steel plug-flow reactors (2.6 mm ID) were loaded with a mixture of 15 − 25 mg of catalyst (75 − 150 μm) and 100 mg SiC diluent (212 − 425 μm). The catalysts were reduced in situ at 350 °C for 8 h (1 °C min^{-1}) in 25 vol% H_2 in He flow at 1 bar. Subsequently, the reactors were cooled to 180 °C and the pressure was increased to 20 bar under H_2 flow. Synthesis gas with H_2/CO = 2 (v/v), 5 vol% He as internal standard and GHSV = 5950–8900 h^{-1} was introduced and the reactors were heated to 220 °C with 1 °C min^{-1}. The reaction products were analyzed online with an Agilent 7890A GC. The hydrocarbon products were separated on an Agilent J&W PoraBOND Q column using a programmed temperature and pressure program with He as carrier, and the hydrocarbons were analyzed by an FID. The permanent gasses were separated on a ShinCarbon ST column, using the same temperature program as for the hydrocarbons and a separate pressure program with Ar as carrier. The permanent gasses were quantified using a TCD. Catalytic activity was reported as CO conversion (X_{CO}), cobalt-time yield (CTY) and turnover frequency (TOF). The selectivity (in $\%_C$) to C_1-C_4 hydrocarbons was determined as $S_{C1\text{-}C4} = 100 \cdot F_{Cn} \cdot n \cdot (F_{CO,in} \cdot X_{CO})^{-1}$ with n being the carbon number of the products and F the flow of the hydrocarbon or CO. The selectivity to C_{5+} hydrocarbons was calculated as $S_{C5+} = 100\ \%_C - S_{C1\text{-}4}$.

3. Results and discussion

3.1. CNT oxidation

Pristine CNT were oxidized using nitric acid to introduce O-containing functional groups and defects in the CNT surface. An increase in acidic groups was found (Table 1) with values similar to what has been obtained previously in our group using gas phase oxidation (~0.5 mmol·g^{-1} acidic groups) [13]. In addition, the structure of CNT and oxCNT was investigated using N_2-physisorption (Table 1, isotherms in Fig. S1). The specific surface area increased by 50 m^2 g^{-1} as a result of the functionalization, probably due to surface roughening and the creation of defects. It should be noted that the actual total pore volume of CNT and oxCNT is probably higher than reported here, as the largest macropores are not probed with N_2-physisorption. The pore volume, determined at p/p_0 = 0.995, was somewhat lower for oxCNT showing that the oxidation treatment had not brought about opening of the inner tubes of the CNT. Overall, these results were well in line with previous reports [13,20].

Table 1
Structural properties of the pristine and functionalized CNT. The number of acidic groups was determined by titration and the structural properties of the CNT by N_2-physisorption.

Support material	Acidic groups (mmol·g^{-1})	BET (m^2·g^{-1})	Pore volume (mL·g^{-1})
CNT	0.02	198	1.5
oxCNT	0.72	248	1.3

3.2. CoO-NC synthesis

Metallic Co-NC were synthesized, exposed to air to allow oxidation to CoO and analyzed using TEM (Fig. 1a,b). The NC were rather spherical and the surface-volume averaged size (D[3,2]) of the NC was consistently between 6 − 7 nm with a standard deviation below 1 nm.

3.3. Catalyst preparation

Model catalysts were prepared by attaching CoO-NC to CNT and oxCNT through impregnation with a colloidal suspension. The cobalt loading of the catalysts was ~10 wt%, as determined by ICP-OES (Table 2), and the catalysts were imaged by TEM (Fig. 1c-d). The CoO-NC were uniformly distributed over oxCNT and appeared somewhat more clustered on CNT. In both cases, the NC were predominantly located on the external surface of the CNT. Analysis of the surface-volume averaged particle sizes (Table 2) revealed that the CoO-NC sizes of 6 − 7 nm was unchanged after attachment.

The crystal structure of the NC was investigated with XRD (Fig. 2a, Table 2). The 6 − 7 nm NC consisted of multiple CoO crystallite domains of 2.2 nm on average, which was caused by the low-temperature oxidation treatment directly after their synthesis, as shown before [27].

3.4. Reduction

Reduction of the pristine samples was investigated using TPR (Fig. 2b). The CoO-NC were reduced in a single step to Co° (single sharp peak), in contrast to a two-step reduction of Co_3O_4/CNT that is often reported (Co_3O_4 to CoO and CoO to Co°) [13,20]. Reduction of CoO occurred at 75 °C higher temperature with support functionalization. Furthermore, the broad feature around 350 °C for CoO-NC/oxCNT could be related to reduction of oxygen-containing functional groups, defective carbon or cobalt species associated to those, as this contribution was absent in the CNT-supported sample. Finally, the high-intensity peak around 600 °C for CoO-NC/oxCNT was assigned to cobalt-catalyzed methanation of the support [27], which did not occur for CoO-NC/CNT in the investigated temperature range. The cause for the difference in CNT methanation behavior was not established, but might be related to different levels of interaction between the Co-NC and support. Furthermore, the degree of reduction (DOR) of CoO was determined from the integral of the peak(s) at 350 °C (CoO-NC/CNT) and 350 and 425 °C (CoO-NC/oxCNT). On CNT, the DOR was 99 %, while it was only 46 % on oxCNT. Overall, the different reduction behavior implied stronger interaction of the NC with oxCNT than with pristine CNT.

The catalysts after reduction at 350 °C for 8 h in 25 vol% H_2 in He and passivation were investigated using TEM and STEM-HAADF combined with EDX (Fig. 3). The NC on CNT grew to 11 nm on average, while those on oxCNT grew only marginally to 8 nm. Thus, functionalization of CNT invoked higher stability of the particles during reduction, probably through more uniform distribution of the NC and/or stronger anchoring of the cobalt particles to the support [20,31]. Stronger anchoring could be related to the lower DOR on oxCNT, as lower reducibility will most likely lead to remaining oxide that will interact more strongly to the oxygen-containing oxCNT surfaces. Furthermore, ~3 nm particles were observed on oxCNT after reduction and passivation, which were absent in the as-prepared state (Fig. S2). This meant that re-dispersion of Co had taken place most likely during reduction and/or passivation. The observation of small particles could be linked to the lower DOR derived from TPR (Fig. 2b), as cobalt oxide

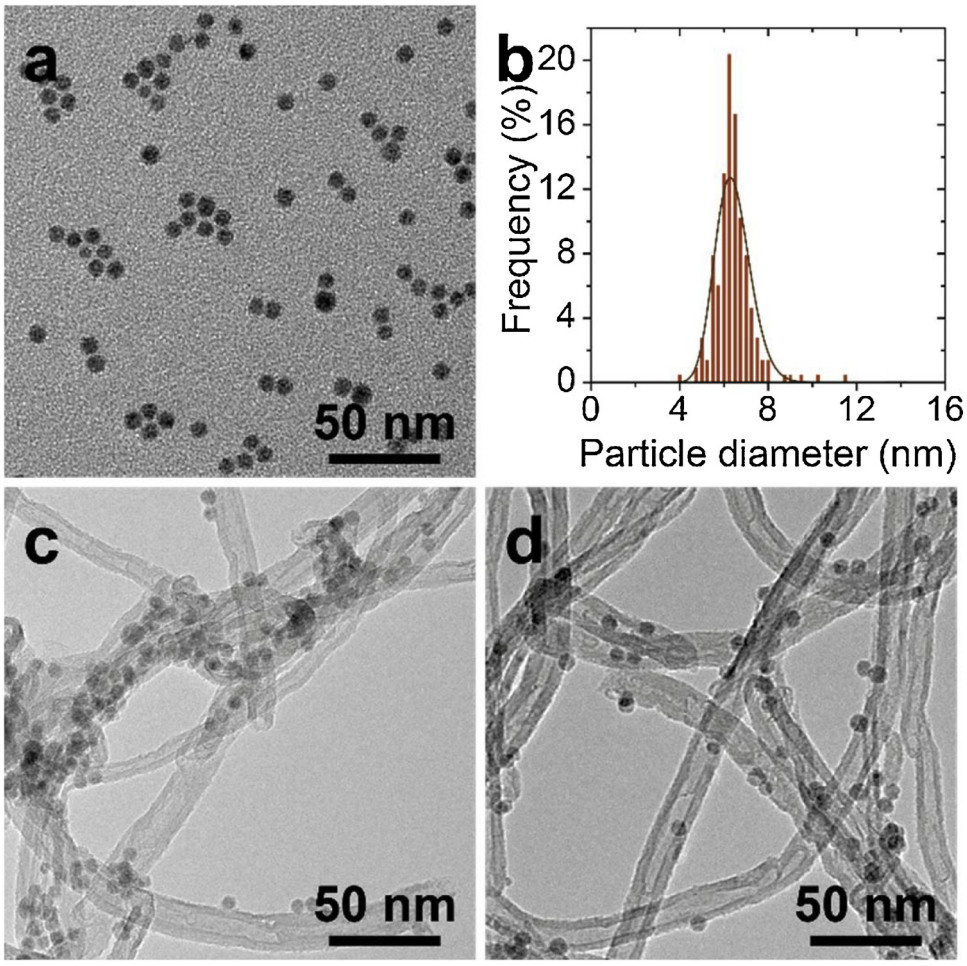

Fig. 1. TEM results of as-synthesized CoO-NC and the CNT- and oxCNT supported samples after NC attachment and drying. (a) TEM image of CoO-NC with a Co-equivalent surface-volume averaged size ($D[3,2]_{Co}$) of 6.5 ± 0.9 nm and (b) the corresponding particle size distribution with lognormal distribution. TEM images of CoO-NC deposited on (c) CNT and on (d) oxCNT.

Table 2
Properties of the as-prepared samples.

Sample	Metal loading (wt %)[a]	$D[3,2]_{Co}$ (nm)[b]	Average crystallite size (nm)[c]
CoO-NC/CNT	9.7	5.9 ± 1.0	2.2 (CoO)
CoO-NC/oxCNT	9.6	6.7 ± 1.3	2.2 (CoO)

[a] Metal loading determined with ICP-OES.
[b] Particle size analysis from TEM of NC after attachment to (ox)CNT.
[c] Average crystallite size derived from XRD.

particles below 4 nm are more difficult to reduce [32–34]. Finally, HR-TEM revealed that the cobalt particles were not covered by carbon and that attachment of the NC to the support appeared similar for both catalysts after reduction and passivation (Fig. S3).

3.5. Fischer-Tropsch synthesis

The cobalt-weight-based activity (cobalt-time yield, CTY) of the catalysts was evaluated over 100 h on stream (Fig. 4). After the initial 20 h on stream, the activity of Co-NC on CNT was substantially higher than on oxCNT. Co-NC/CNT was remarkably active, since CTY values of $26{\cdot}10^{-5}$ $mol_{CO}{\cdot}g_{Co}^{-1}{\cdot}\ s^{-1}$ at the prevailing reaction conditions are rarely reported in literature for non-promoted cobalt catalysts. Furthermore, the activity profile of Co-NC/CNT was quite stable after the initial period of 20 h on stream, while the Co-NC/oxCNT deactivated more rapidly.

During the initial 20 h on stream, both catalysts first activated rapidly before deactivation took over. Activation could be caused by loss of residual ligands under FT conditions through extraction by the formed reaction products. When omitting this strong activation, extrapolation to 0 h gave approximately the same activity for both catalysts and the difference in activity on both supports only set in later. The same was evident from the evolution of C_{5+}-selectivity of the NC-based catalysts with time-on-stream (Fig. S4), i.e. initially similar selectivity that later diverged to 82 % on CNT and 78 % on oxCNT, qualitatively in line with previous literature [13]. These results suggest that differences in catalytic performance take several hours to develop under FT conditions.

The catalytic results obtained after ~90 h on stream are summarized in Table 3. The cobalt-weight-based activity is reported both as initial and final CTY. Furthermore, surface-volume averaged cobalt particle sizes in the spent and passivated state after > 100 h on stream were determined by TEM (Table 3, Fig. S5). Very few particles larger than 20 nm were observed and omitted in the particle size analysis.

The cobalt particle sizes of used catalysts were compared to those of the catalysts in the pristine and reduced state to show the evolution of particle size (Fig. 5a). On pristine CNT, growth of the initially 6 nm NC had occurred during reduction and the average size after FT was 10 nm. In contrast, the average NC size on oxCNT remained constant at 7 − 8 nm during reduction and FT and the particle size distribution was close to its original form (Fig. S2). Overall, oxidation of CNT prevented average growth of the Co-NC during reduction/FT, probably because of a stronger interaction between Co and oxCNT. This is in line with

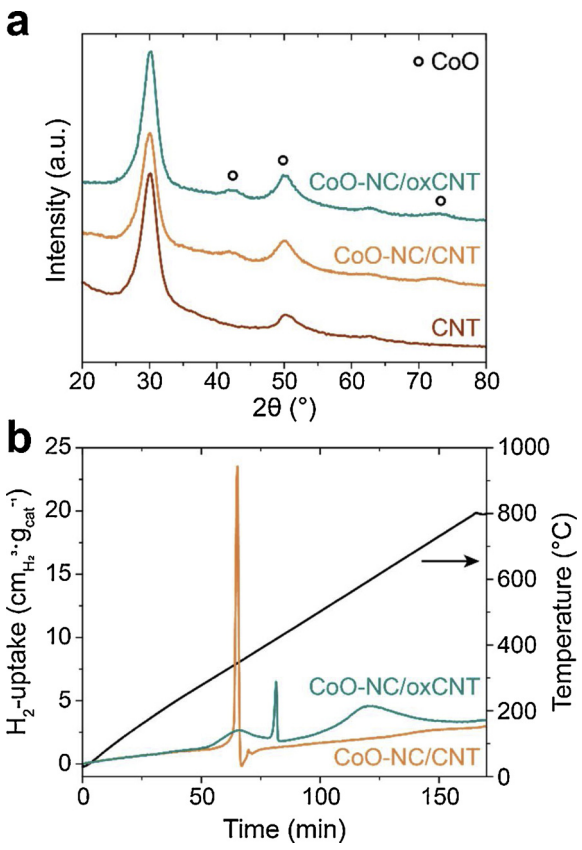

Fig. 2. (a) Ex situ XRD patterns of CNT and the as-prepared samples. (b) TPR of the CoO-NC/CNT and CoO-NC/oxCNT in 5 % H_2 in Ar with a heating ramp of 5 °C min^{-1}.

literature, as similar or higher stability of Co on oxCNT was reported before [13,20].

The average particle sizes were used to calculate the cobalt-specific metallic surface areas. From these areas, cobalt-surface-based activities (turnover frequencies, TOF) after 100 h on stream were derived using the final CTY and particle size of the spent catalyst (Table 3). Comparison of the final TOF showed that Co-NC on CNT ($150{\cdot}10^{-3}$ s^{-1}) were significantly more active than on oxCNT ($63{\cdot}10^{-3}$ s^{-1}). In fact, Co-NC/CNT was exceptionally active, considering that TOF values between $10{\cdot}10^{-3}$ s^{-1} and $100{\cdot}10^{-3}$ s^{-1} are typically obtained [27].

The TOF was calculated as well for the initial stage of the reaction using the initial (maximal) CTY and particle size of the catalysts after reduction. The TOF decreased from the initial to the final stage of the reaction by 19 % for Co-NC/CNT and by 47 % for Co-NC/oxCNT. Hence, deactivation was predominantly caused by declining intrinsic activity over the course of the reaction and not by particle growth.

As a potential explanation for differences in catalytic performance, we investigated the crystal structure of cobalt in the NC-based catalysts during reduction and under FT conditions using in situ XRD at 10 bar, 220 °C and an H_2/CO ratio of 2 v/v (Fig. 5b, refined patterns in Fig. S6). The data was analyzed using Rietveld refinement. To improve the refinement results, it was necessary to include preferred orientations of hcp Co crystallites. Rather than having anisotropic crystallites (for which no evidence was observed in TEM), we propose that this was caused by an intergrown Co^0 structure. XRD analysis of metallic cobalt can be complicated by stacking faults and the extent to which these are present depends strongly on the catalyst synthesis and treatments [21,35]. Our refinement using only hcp and fcc Co phases did not account for an intergrowth structure, but did accommodate much of its features by increasing the intensity of the hcp Co (0002) peak, therefore possibly overestimating the fraction of hcp Co.

The width of the peaks between 18 and 25° 2θ was the main difference between the diffraction patterns of Co-NC on CNT and oxCNT and is related to Co^0 crystallite size (Fig. 5b). Especially for Co-NC/CNT, satisfying refinement results were not obtained using a combination of an hcp and fcc phase (Fig. S6), probably due to a highly intergrown Co^0 structure. The pattern of the Co^0 phase on CNT did bear a strong resemblance to spherical 10 nm Co^0 crystallites reported by Sławiński et al. [35] with a hcp-fcc stacking probability of 0.5, i.e. random stacking. In our case, an average crystallite size of 9.9 nm was also found for the fcc phase, whereas the hcp Co crystallites were only 4.0 nm. This small size of hcp Co was most likely an artefact caused by inefficient modeling of the intergrowth structure. Therefore, the Co^0 crystallites were estimated to be approximately 10 nm in line with literature [35] and TEM results, assuming monocrystalline Co-NC. In comparison, the pattern of Co-NC/oxCNT could be modelled better and the average sizes of hcp and fcc Co domains were only 2.9 and 3.9 nm, respectively. As this is smaller than the average particle size from TEM, it meant that polycrystalline Co-NC were formed on oxCNT upon reduction. Furthermore, neither appreciable differences in hcp/fcc ratio nor significant amounts of crystalline CoO were detected.

More crystalline Co^0 appeared present on CNT than on oxCNT, as evidenced by the higher integral between 18–25 ° 2θ. Rietveld refinement indicated a crystalline phase composition of Co-NC/CNT of 8.8 wt % Co^0 and 91.2 wt% CNT, close to the value from ICP (9.7 wt% Co, Table 2). In the case of Co-NC/oxCNT, the crystalline Co^0 phase was only 6.1 wt% with 93.9 wt% oxCNT, while its nominal cobalt content from ICP was 9.6 wt%. Oxidation of CNT thus resulted in less crystalline cobalt in the active catalyst, which is qualitatively in line with observations by Chernyak et al. [36]. It is unsure whether the remaining amorphous cobalt was present in ionic or metallic form. Nevertheless, the 32 % lower crystallinity of metallic Co for Co-NC/oxCNT matched very well with its 36 % lower initial TOF suggesting that differences in crystalline Co^0 caused the difference in initial TOF.

The diffraction patterns did not change from the final stage of reduction to 40 h on stream under FT conditions (Fig. S7). Hence, restructuring or growth of the crystalline Co phase during FT was unlikely, meaning that deactivation occurring on oxCNT (Fig. 4) had a different origin than changing crystal structure and size. Yu et al. [31] observed a similar strong deactivation of Co on oxidized CNF. However, they ascribed the deactivation to oxidation of Co^0 during FT, which our in situ XRD results did not reveal. In our case, a possible explanation for the deactivation could be enhanced deposition of carbonaceous species [37] under the influence of defects/oxygen groups on CNT or amorphous cobalt, as has been observed before on oxidized CNT [36], but this would require further research. Overall, precise synthesis of Co-NC of a particular size combined with uniform attachment to both supports resulted in very similar as-prepared catalysts, varying only in the CNT surface composition. These proved to be excellent model systems to investigate the effect of CNT functionalization on FT in detail.

4. Conclusions

We have investigated the impact of surface oxidation of carbon nanotube (CNT) supports on the structure and performance of cobalt nanocrystals (Co-NC) in the Fischer-Tropsch (FT) synthesis. Well-defined 6 nm colloidal CoO-NC were synthesized and attached to CNT or oxidized CNT (oxCNT) with a loading of 10 wt% Co. After reduction and passivation, NC growth and complete reduction of the NC were observed on CNT, while growth was absent on oxCNT and only ~50 % CoO reduction was obtained. The turnover frequency (TOF) of the Co-NC after 100 h of FT was exceptionally high on CNT with $150{\cdot}10^{-3}s^{-1}$ against $63{\cdot}10^{-3}s^{-1}$ oxCNT. Using in situ XRD, 32 % less crystalline metallic cobalt was found on oxidized CNT under FT conditions, probably causing the 35 % lower initial TOF compared to Co-NC/CNT. Furthermore, the Co-NC on oxCNT deactivated more, which could not be explained by particle growth, NC restructuring, or oxidation during

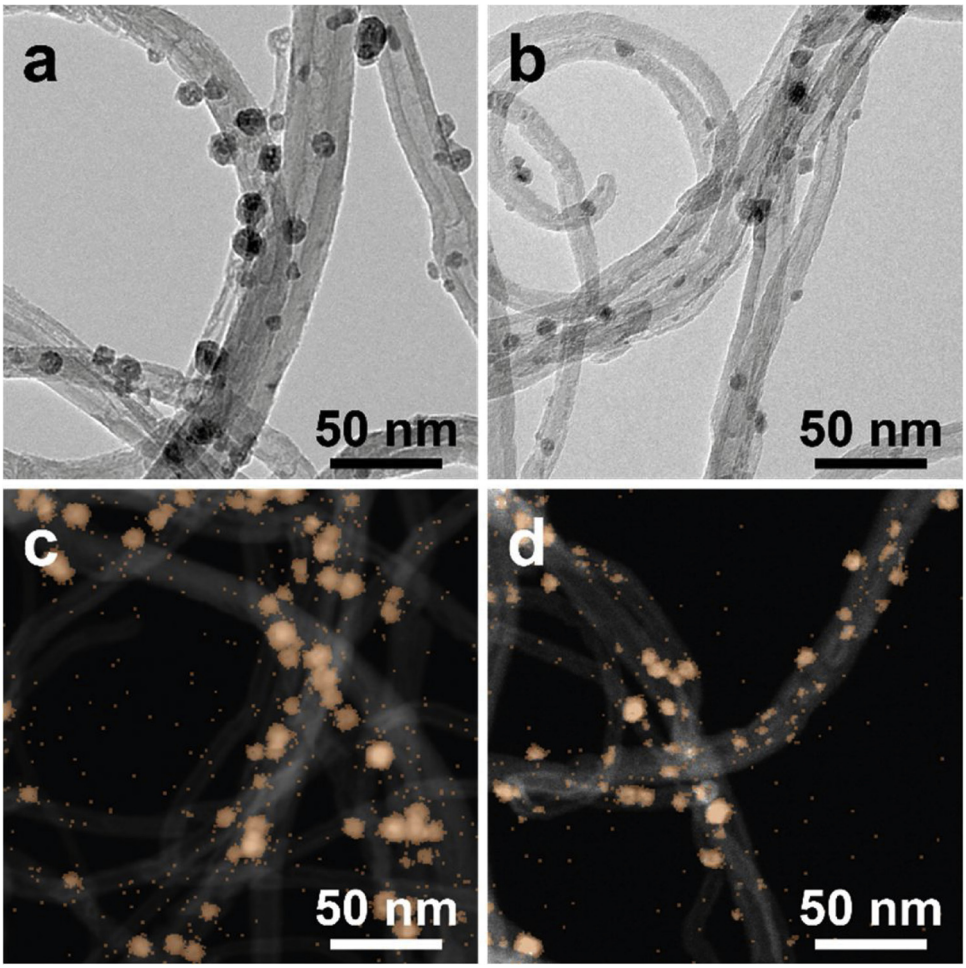

Fig. 3. Electron microscopy of the catalysts after reduction at 350 °C and passivation. TEM results of (a) Co-NC/CNT and (b) Co-NC/oxCNT are shown together with STEM-HAADF results including cobalt EDX maps of (c) Co-NC/CNT and (d) Co-NC/oxCNT. The cobalt signal is shown in orange.

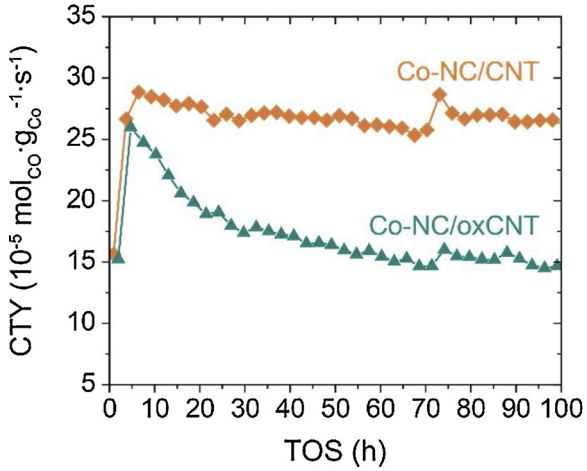

Fig. 4. Cobalt-time yield of Co-NC/CNT and Co-NC/oxCNT during 100 h on stream at 20 bar, 220 °C, $H_2/CO = 2$, GHSV = 5950–8900 h^{-1} and CO conversion levels between 15 and 40 %.

FT, leaving enhanced deposition of carbonaceous species as a probable cause. This study illustrates the potential of nanocrystal-based model catalyst synthesis for the investigation of structure-performance relationships.

CRediT authorship contribution statement

T.W. van Deelen: Conceptualization, Methodology, Software, Formal analysis, Validation, Investigation, Writing - original draft, Visualization, Project administration. **H. Yoshida:** Methodology, Software, Formal analysis, Investigation, Writing - review & editing, Funding acquisition. **R. Oord:** Methodology, Software, Formal analysis, Validation, Investigation, Writing - review & editing. **J. Zečević:** Methodology, Resources, Writing - review & editing, Funding acquisition. **B.M. Weckhuysen:** Resources, Writing - review & editing, Funding acquisition. **K.P. de Jong:** Conceptualization, Methodology, Formal analysis, Resources, Writing - review & editing, Visualization, Supervision, Project administration, Funding acquisition.

Acknowledgements

T.W.v.D., B.M.W. and K.P.d.J. acknowledge Shell Global Solutions and the Netherlands Association for Scientific Research (NWO) for funding through the CHIPP framework. H.Y., J.Z. and K.P.d.J. acknowledge the < GS3 > European Research Council < /GS13 > , EU FP7 ERC Advanced Grant no. 338846. H.Y. acknowledges the Program for Advancing Strategic International Networks to Accelerate the Circulation of Talented Researchers by Japan Society for the Promotion of Science (JSPS). We thank Arjan den Otter and Nazila Masoud (N_2-physisorption), Helen de Waard (ICP-OES), and Carlos Hernández Mejía (TPR) for the measurements indicated.

Table 3
Fischer-Tropsch synthesis results obtained at 20 bar, 220 °C, 2 H_2/CO (v/v), GHSV = 5950–8900 h^{-1}. The reported data was averaged between 80 − 96 h on stream unless stated otherwise.

Sample	X_{CO} (%)	$CTY_{initial}$ [a,b]	CTY_{final} [a]	$TOF_{initial}$ (10^{-3} s^{-1}) [b,c]	TOF_{final} (10^{-3} s^{-1}) [d]	S_{C1} (%C)	S_{C5+} (%C)	$D[3,2]_{Co,\ spent}$ (nm) [e]
Co-NC/CNT	25	29	26	190	150	11	82	9.6 ± 2.9
Co-NC/oxCNT	23	26	15	120	63	12	78	7.2 ± 1.6

[a] In (10^{-5} $mol_{CO} \cdot g_{Co}^{-1} \cdot s^{-1}$).
[b] Reported at maximum CTY between 0 − 10 h on stream.
[c] Based on the metallic surface area calculated from the average Co particle size of the reduced and passivated catalyst.
[d] Based on the metallic surface area calculated from the average Co particle size of the spent and passivated catalyst.
[e] Determined by TEM; very few large particles (> 20 nm) were excluded, if present.

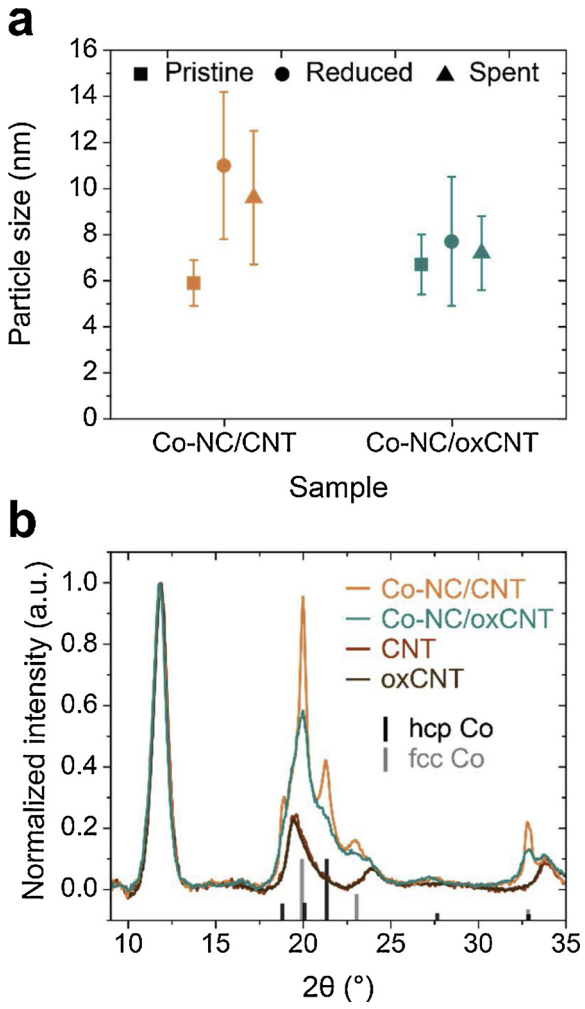

Fig. 5. Evolution of Co particle size and Co crystal structure under FT conditions. (a) Average particle sizes ($D[3,2]_{Co}$) determined by TEM of the catalysts in the as-prepared, reduced and passivated, and spent and passivated state. The error bars indicate the standard deviation. (b) Background-subtracted and normalized diffraction patterns of Co-NC on CNT and oxCNT during FT as obtained with in situ XRD and subsequent Rietveld refinement. The diffractograms were obtained between 32 and 42 h on stream at 10 bar, 220 °C and H_2/CO = 2 v/v by accumulating five scans of 2 h. No change in the diffraction patterns was apparent over the course of the reaction. Reference patterns of the bare supports were measured at ambient conditions. Contributions from the background and amorphous phases were determined using Rietveld refinement (Fig. S7), subtracted from the experimental patterns, and the residual patterns were normalized to the maximum intensity of the CNT (002) peak at 12° 2θ. Bars represent reference patterns of hcp Co (PDF 04-001-3273) and fcc Co (PDF 04-001-2681).

Appendix A. Supplementary data

Supplementary material related to this article can be found, in the online version, at doi:https://doi.org/10.1016/j.apcata.2020.117441.

References

[1] R.C. Armstrong, C. Wolfram, K.P. de Jong, R. Gross, N.S. Lewis, B. Boardman, A.J. Ragauskas, K. Ehrhardt-Martinez, G. Crabtree, M.V. Ramana, Nat. Energy 1 (2016) 15020.
[2] BP, BP Energy Outlook 2018, (2018) (accessed 19 September 2019), http://www.bp.com/content/dam/bp/business-sites/en/global/corporate/pdfs/energy-economics/energy-outlook/bp-energy-outlook-2018.pdf.
[3] A.Y. Khodakov, W. Chu, P. Fongarland, Chem. Rev. 107 (2007) 1692–1744.
[4] E. van Steen, M. Claeys, K.P. Möller, D. Nabaho, Appl. Catal. A Gen. 549 (2018) 51–59.
[5] Short-Term Energy Outlook December 2018, U.S. Energy Information Administration, 2018 (accessed 19 September 2019), https://www.eia.gov/outlooks/steo/archives/dec18.pdf.
[6] L. Lefferts, E.J.M. Hensen, J.W. Niemantsverdriet, U. Hanefeld, L. Lefferts (Eds.), Catalysis: An Integrated Textbook for Students, first ed., Wiley-VCH, Weinheim, 2018, pp. 15–71.
[7] P. Munnik, P.E. de Jongh, K.P. de Jong, Chem. Rev. 115 (2015) 6687–6718.
[8] G. Prieto, M.I.S. De Mello, P. Concepción, R. Murciano, S.B.C. Pergher, A. Martinez, ACS Catal. 5 (2015) 3323–3335.
[9] H. Xiong, L.L. Jewell, N.J. Coville, ACS Catal. 5 (2015) 2640–2658.
[10] Y. Yang, L. Jia, B. Hou, D. Li, J. Wang, Y. Sun, J. Phys. Chem. C 118 (2014) 268–277.
[11] G.L. Bezemer, P.B. Radstake, V. Koot, A.J. Van Dillen, J.W. Geus, K.P. De Jong, J. Catal. 237 (2006) 291–302.
[12] G.L. Bezemer, J.H. Bitter, H.P.C.E. Kuipers, H. Oosterbeek, J.E. Holewijn, X. Xu, F. Kapteijn, A.J. van Dillen, K.P. de Jong, J. Am. Chem. Soc. 128 (2006) 3956–3964.
[13] T.O. Eschemann, W.S. Lamme, R.L. Manchester, T.E. Parmentier, A. Cognigni, M. Rønning, K.P. de Jong, J. Catal. 328 (2015) 130–138.
[14] P. Serp, M. Corrias, P. Kalck, Appl. Catal. A Gen. 253 (2003) 337–358.
[15] J.-P. Tessonnier, D. Rosenthal, T.W. Hansen, C. Hess, M.E. Schuster, R. Blume, F. Girgsdies, N. Pfänder, O. Timpe, D.S. Su, R. Schlögl, Carbon 47 (2009) 1779–1798.
[16] T.G. Ros, A.J. Van Dillen, J.W. Geus, D.C. Koningsberger, Chem. Eur. J. 8 (2002) 1151–1162.
[17] J.H. Bitter, J. Mater. Chem. 20 (2010) 7312–7321.
[18] H. Zhang, C. Lancelot, W. Chu, J. Hong, A.Y. Khodakov, P.A. Chernavskii, J. Zheng, D. Tong, J. Mater. Chem. 19 (2009) 9241–9249.
[19] V. Vosoughi, S. Badoga, A.K. Dalai, N. Abatzoglou, Ind. Eng. Chem. Res. 55 (2016) 6049–6059.
[20] S.A. Chernyak, E.V. Suslova, A.S. Ivanov, A.V. Egorov, K.I. Maslakov, S.V. Savilov, V.V. Lunin, Appl. Catal. A Gen. 523 (2016) 221–229.
[21] O. Ducreux, B. Rebours, J. Lynch, M. Roy-Auberger, D. Bazin, Oil Gas Sci. Technol. - Rev. d'IFP Energies Nouv. 64 (2009) 49–62.
[22] M. Sadeqzadeh, H. Karaca, O.V. Safonova, P. Fongarland, S. Chambrey, P. Roussel, A. Griboval-Constant, M. Lacroix, D. Curulla-Ferré, F. Luck, A.Y. Khodakov, Catal. Today 164 (2011) 62–67.
[23] M.K. Gnanamani, G. Jacobs, W.D. Shafer, B.H. Davis, Catal. Today 215 (2013) 13–17.
[24] J.-X. Liu, H.-Y. Su, D.-P. Sun, B.-Y. Zhang, W.-X. Li, J. Am. Chem. Soc. 135 (2013) 16284–16287.
[25] S. Lyu, L. Wang, J. Zhang, C. Liu, J. Sun, B. Peng, Y. Wang, K.G. Rappé, Y. Zhang, J. Li, L. Nie, ACS Catal. 8 (2018) 7787–7798.
[26] F. Zaera, Chem. Soc. Rev. 42 (2013) 2746–2762.
[27] T.W. van Deelen, H. Su, N.A.J.M. Sommerdijk, K.P. de Jong, Chem. Commun. 54 (2018) 2530–2533.
[28] V. Iablokov, S.K. Beaumont, S. Alayoglu, V.V. Pushkarev, C. Specht, J. Gao, A.P. Alivisatos, N. Kruse, G.A. Somorjai, Nano Lett. 12 (2012) 3091–3096.
[29] K.H. Cats, B.M. Weckhuysen, ChemCatChem 8 (2016) 1531–1542.
[30] J. Xie, P.P. Paalanen, T.W. van Deelen, B.M. Weckhuysen, M.J. Louwerse, K.P. de Jong, Nat. Commun. 10 (2019) 167.
[31] Z. Yu, Ø. Borg, D. Chen, E. Rytter, A. Holmen, Top. Catal. 45 (2007) 69–74.

[32] M. Wolf, H. Kotzé, N. Fischer, M. Claeys, Faraday Discuss. 197 (2017) 243–268.
[33] E. van Steen, M. Claeys, M.E. Dry, J. van de Loosdrecht, E.L. Viljoen, J.L. Visagie, J. Phys. Chem. B 109 (2005) 3575–3577.
[34] N.E. Tsakoumis, J.C. Walmsley, M. Rønning, W. van Beek, E. Rytter, A. Holmen, J. Am. Chem. Soc. 139 (2017) 3706–3715.
[35] W.A. Sławiński, E. Zacharaki, H. Fjellvåg, A.O. Sjåstad, Cryst. Growth Des. 18 (2018) 2316–2325.
[36] S.A. Chernyak, E.V. Suslova, A.V. Egorov, K.I. Maslakov, S.V. Savilov, V.V. Lunin, Appl. Surf. Sci. 372 (2016) 100–107.
[37] D. Peña, A. Griboval-Constant, C. Lancelot, M. Quijada, N. Visez, O. Stéphan, V. Lecocq, F. Diehl, A.Y. Khodakov, Catal. Today 228 (2014) 65–76.